Energy, Environmental, and Catalysis Applications

Enhanced and Facet-specific Electrocatalytic Properties of Ag/BiFeO Composite Nanoparticles

Kai Wang, Xiaoguang Xu, Liying Lu, Haicheng Wang, Yan Li, Yong Wu, Jun Miao, Jin Z. Zhang, and Yong Jiang

ACS Appl. Mater. Interfaces, **Just Accepted Manuscript** • DOI: 10.1021/acsami.8b01148 • Publication Date (Web): 22 Mar 2018

Enhanced and Facet-specific Electrocatalytic Properties of $Ag/Bi_2Fe_4O_9$ Composite Nanoparticles

Kai Wang,[†] Xiaoguang Xu,*[,†] Liying Lu,[‡] Haicheng Wang, [§,∥] Yan Li,[†,#] Yong Wu,[†] Jun Miao,[†] Jin Zhong Zhang,[#] Yong Jiang,*[,†]

[†]*School of Materials Science and Engineering, University of Science and Technology Beijing, Beijing 100083, China*

[‡]*School of Chemistry and Biological Engineering, University of Science and Technology Beijing, Beijing 100083, China*

[§]*National Center for Materials Service Safety, University of Science and Technology Beijing, Beijing 100083, China*

[∥] *Materials Sciences Division, Lawrence Berkeley National Laboratory, Berkeley, CA 94720, USA*

[#] *Department of Chemistry & Biochemistry, University of California, Santa Cruz, CA 95064, USA*

ABSTRACT: $Ag/Bi_2Fe_4O_9$ nanoparticles (BFO NPs) have been synthesized using a two step approach involving glycine combustion and visible light irradiation. Their structures were characterized in detail using XRD, TEM, SEM, and STEM techniques. Their electrocatalytic properties were studied through enzymatic glucose detection with an amperometric biosensor. The Ag deposited on selective crystal facets of BFO NPs significantly enhanced their electrocatalytic activity. To gain insight into the origin of the enhanced electrocatalytic activities, we have carried out studies of Ag^+ reduction and Mn^{2+} oxidation reaction at {200} and {001} facets, respectively. The results suggest effective charge separation on the BFO NP surfaces, which is likely responsible for the enhanced electrocatalytic properties. Furthermore, the enhanced ferromagnetism was

* Corresponding authors: E-mail: xgxu@ustb.edu.cn (X.G. Xu), yjiang@ustb.edu.cn (Y. Jiang)

observed after the Ag deposition on BFO NPs, which may be related to the improved electrocatalytic properties through spin-dependent charge transport. The facet-specific electrocatalytic properties are highly interesting and desired for chemical reactions. This study demonstrates that Ag/BFO NPs are potentially useful for electrocatalytic applications including biosensing and chemical synthesis with high product selectivity.

KEYWORDS: Ag/$Bi_2Fe_4O_9$; nanoparticle; electrocatalytic properties; ferromagnetism; spin-dependent transport; facet-specific deposition.

1. INTRODUCTION

$Bi_2Fe_4O_9$ (BFO) is a ferroelectric and antiferromagnetic semiconductor that absorbs visible light.[1-3] In orthorhombic BFO, iron cations are evenly distributed between the tetrahedral and octahedral positions, while bismuth cations are coordinated by eight oxygen ions.[4,5] However, bond length of Bi-O is sensitive to the synthesis condition and induces the changes of the coordination state of Bi^{3+} due to the stereo-chemically active lone pair electron.[6,7] BFO is paramagnetic at room temperature, and undergoes a phase transition to an antiferromagnetic state at 264 K.[8,9] Also, BFO particles with size ranging from nanometer to micrometer and large surface area have been synthesized and utilized for gas sensing [10] and multiple catalysis.[11,12]

In particular, BFO nanoparticles (NPs) with large surface-to-volume ratio are promising as multifunctional materials for catalysis as well as sensing applications.[13,14] However, the low conductivity of BFO limits its applications. To address this issue, Li *et al*. used Ag^+ and Mn^{2+} ions deposited on different facets of $BiVO_4$ to capture the photo-generated electrons and holes so as to reduced their recombination and thereby improve conductivity.[15] This work seems to indicate it is possible to use the negative charges accumulated on the ferroelectric BFO NPs surfaces to reduce Ag^+ ions to generate metallic Ag NPs that can, in turn, be used to enhance the electrocatalytic property of BFO NPs by improving conductivity.

Biosensing nanomaterials are hotly pursued in recent years for detecting important biological samples such as DNA, proteins, glucides and heavy metals.[16-18] The sensitivity and linearity of biosensing are important for practical applications. Inorganic metal oxides have been good candidates for biosensing due to their high stability and low cost. For example, TiO_2-based, ZnO-based and Graphene-Coated nanostructures, such as ZnO@ZnS, ZnO-NiO, CS-ZnO, nitrogen-doped graphene (NG) and NG/Ag have been used for detecting important molecules such

as glucose and uric acid,[19-23] and demonstrated good stability, reproducibility and electrocatalytic activity. However, there is still urgent need to develop new materials with improved electrocatalytic properties and enhanced signals.[24-26]

Glucose monitoring is extremely important, especially for patients with diabetes.[27,28]Amperometric enzyme electrodes, based on Glucose oxidase (GOD), have been widely used in the determination of glucose due to their high sensitivity, repeatability and ease of operation.[19] In a GOD-based glucose biosensor, glucose is catalyzed by GOD and oxidized into gluconolactone, as shown in the following:

$$GOD_{ox} + Glucose \rightarrow Gluconolactone + GOD_{red} \quad (1)$$

$$GOD_{red} + O_2 \rightarrow GOD_{ox} + H_2O_2 \quad (2)$$

One of the reaction products H_2O_2 should be decomposed at the electrode to release electrons, so that the current detected is proportional to the concentration of glucose.[29]

In this paper, we report on the synthesis of Ag/BFO composites, in which Ag NPs are selectively deposited onto the {200} facets of BFO NPs. The nanocomposites were characterized using XRD, TEM, STEM, XPS, and electrochemical techniques. Deposition of the Ag NPs significantly enhanced the electrocatalytic activity of the BFO NPs, as successfully demonstrated in the enzymatic detection of glucose. The enhanced electrocatalytic properties are attributed to the improved charge separation at the different facets of BFO NPs, as well as spin-dependent electron transport. Furthermore, the facet dependence is highly interesting and potentially useful for different applications for which reaction product selectivity is important.

2. EXPERIMENTAL SECTION

Materials. All the reagents were of analytical grade and used without further purification. GOD type VII was purchased from Sigma. Nafion was purchased from E. I. Du Pont Company. 10

mmol·L^{-1} phosphate buffer saline (PBS) sol was prepared by dissolving NaH_2PO_4 and Na_2HPO_4 into distilled water. GOD solution was prepared by dissolving the GOD powder (25.0 mg) into 10 mmol·L^{-1} PBS solution (250 mL) at pH value of 7.2.

Glycine Combustion Synthesis of BFO. $Bi(NO_3)_3·5H_2O$ (5.0 mmol), $Fe(NO_3)_3·9H_2O$ (10 mmol) with a 1:2 molar ratio were dissolved into 15.0 mL of 2.0 mol·L^{-1} HNO_3 solution. When the reactants have been completely dissolved, 150 mmol glycine was added into the precursor solution with a 15:1 molar ratio of glycine to Fe ions. The solution was stirred with a magnetic stirrer to make the glycine dissolve completely and get red solution. Then, the solution was heated at 150 ^oC with constant magnetic stirring. After flaming, brown powders were obtained. The brown particles were heated to 200 ^oC at a step of 5 ^oC/min starting from room temperature and kept at 200 ^oC for 20 min. Then the particles were heated to 650 ^oC at the same heating rate and annealed for 2 h. After annealing, the particles were furnace cooled to room temperature.

Hydrothermal Synthesis of BFO. $Bi(NO_3)_3·5H_2O$ (5.0 mmol) and $Fe(NO_3)_3·9H_2O$ (10 mmol) with a 1:2 molar ratio were dissolved into 15.0 mL of 2.0 mol·L^{-1} HNO_3 solution. Then, 50 mL KOH solution (2.0 mol·L^{-1}) was added dropwise into the solution until Bi^{3+} and Fe^{3+} were deposited completely. The brown precipitates were washed by distilled water for 3 times, and then mixed with 40 mL of NaOH solution (12 mol·L^{-1}). After stirring for 1 h, the suspension was transferred into a 50 mL autoclave with Teflon liner. Hydrothermal treatment was carried out at 180 ^oC for 24 h. Finally, the autoclave was cooled down to room temperature. The brown products were filtered and washed with deionized water and ethanol until the precipitates are neutral, and dried at 80 ^oC for four hours.

Facet-selective Photo-synthesis of Ag/BFO, Mn_2O_3/BFO and Ag/Mn_2O_3/BFO particles. Considering that the coexistence of two kinds of facets is an important factor for selective

photo-deposition, we chose the BFO particles synthesized by hydrothermal synthesis as precursor to provide regular crystal facets for Ag and Mn_2O_3 deposition. 0.50 g of precursor ($AgNO_3$ or $MnSO_4$) was dissolved in 100 mL deionized water. Subsequently, 0.30 g BFO particles were added into the solution. Suspension was then stirred with or without irradiation by an iodine tungsten lamp. After 10 hours photo-deposition, the suspension was filtered, washed with deionized water and ethanol for more than six times, and finally dried at 80 ^oC for 4 hours. For the preparation of Ag/Mn_2O_3/BFO composites, 0.50 g $MnSO_4$ was dissolved in 100 mL deionized water, and then 0.30 g Ag/BFO particles was put into the solution. Then, Ag/Mn_2O_3/BFO composites and Ag/BFO NPs synthesized by glycine combustion can be obtained through the above steps. It is worth noting that the BFO and Ag/BFO NPs used in glucose detection were synthesized by glycine combustion synthesis to ensure a small crystal size with correspondingly large specific surface area.

Preparation of Nafion/GOD/BFO/ Glassy Carbon Electrode (GCE). The pretreated GCE with a diameter of 5 mm was polished with alumina slurries, and sonicated with acetone, deionized water and ethanol. To fabricate the glucose biosensor electrode, 40.0 mg of the prepared NPs were dispersed in 10.0 mL ethanol, and sonicated for 15 min. Then 5.0 μL suspension was dropped on the electrode. 2.0 μL of GOD solution was dropped on the BFO NPs/GCE electrode and dried in air. Subsequently, 2.0 μL of 0.5% Nafion solution was dropped on the GOD/BFO/GCE electrode and dried at room temperature to form a protective film. The prepared electrode was stored in refrigerator at 4 ^oC. The BFO and Ag/BFO NPs loaded on the electrodes are calculated to be 20 μg.

Characterization. The X-ray diffraction (XRD) patterns were measured using an Ultima IV diffractometer (Cu-Kα radiation, λ = 0.15406 nm, 40 KV, 40 mA). The Rietveld refinement was carried out using the Fullprof Suite package. The specific surface areas of the materials were determined using the Brunauer-Emmett-Teller (BET) method at liquid nitrogen temperature using a

MicroActive for ASAP 2460 analyzer. Field-emission scanning electron microscope (FESEM) was investigated on a Zeiss Supra 55 SEM at 3.0 kV accelerating voltage. Transmission electron microscope (TEM) and high resolution transmission electron microscope (HRTEM) were performed on a JEOL JEM-2010 with an accelerating voltage of 200 kV. Scanning transmission electron microscope energy dispersive spectrometer (STEM-EDS) was performed on a STEM FEI TitanX at 200 kV equipped with a SuperX windowless EDS detector. The X-ray photoelectron spectra (XPS) were measured on a Kratos Axis Ultra DLD spectrometer with monochromatic Al Kα radiation (hν = 1486.6 eV). The compositions of Ag/BFO NPs were determined by inductively coupled plasma optical emission spectroscopy (ICP-OES, Agilent 725). The magnetic hysteresis loops were measured over a field range of ±2.0 T at room temperature with Physical Property Measurement System (PPMS, Quantum Design PPMS-9). The electrochemical experiment was implemented at room temperature by using CHI 600C electrochemical workstation with a three-electrode system: GCE/(Ag/BFO)/GOD/Nafion electrode used as a working electrode, Ag/AgCl as a reference electrode and platinum electrode as a counter electrode.

3. RESULTS AND DISCUSSION

3.1. Crystal Structures of BFO Particles. Figure 1 shows the XRD patterns of the BFO particles fabricated by the hydrothermal and glycine combustion methods, respectively, as well as that of the Ag/BFO NPs synthesized by glycine combustion. All diffraction peaks of the BFO samples can be well indexed to orthorhombic BFO in Pbam space group (JCPDS 25-0090), indicating a high crystallinity. The lattice parameters of the BFO NPs and Ag/BFO NPs synthesized by glycine combustion were carried out by Rietveld refinement and the lattice parameters together with the corresponding expansion coefficients are presented in Figures S1 and S2 (see supplementary material). According to the Rietveld refinement results, the lattice parameters of

BFO NPs were calculated to be a = 7.964 Å, b = 8.449 Å, and c = 6.003 Å, which are well consistent with the data presented in JCPDS 25-0090.[8] The lattice parameters have no obvious change after the Ag deposition. To decide the effect of the Ag deposition on the crystal structure of BFO NPs, it is necessary to measure the concentration of Ag in Ag/BFO NPs. The ICP-OES measurements show that the weight ratio of Ag in Ag/BFO NPs is only 0.21%, which suggests the little Ag contribution to the XRD pattern. Therefore, we have characterized the crystal structure of Ag/BFO NPs by XPS and TEM methods.

The morphologies and diffraction spots of the BFO particles were studied using TEM, with results shown in Figure 2. The BFO particles synthesized by hydrothermal method has a uniform cuboid shape (Figure 2a), which is the most commonly observed for BFO particles.[30, 31] According to the TEM images, the BFO particles are around 1.0 μm in both length and width, and 200 nm in thickness. As shown in Figure 2b, the BFO particles are irregularly spherical nanoparticles with a diameter of about 60 nm. Similar BFO NPs have been demonstrated to have high photocatalytic efficiency for methyl orange degradation.[32] Nevertheless, the BFO particles synthesized by hydrothermal method have some unique features, e.g. various highly uniform crystal facets, as shown in Figure 2c, that reveals both (200) and (121) crystal facets. In contrast, the BFO NPs from glycine combustion exhibit (001) and (110) crystal facets as indexed in Figure 2d. The diffraction spots shown in Figures 2e and 2f further confirm the different crystal facets of the two kinds of BFO particles synthesized differently. The angle between the (200) and (121) crystal facets is about 65^{o} as shown in Figure 2e, which indicates the side surface of the BFO particles is the (200) crystal facet. Combined with the TEM images of other parts of the BFO particles synthesized by hydrothermal method shown in Figure S3 and S4, the appearance of the (121) facet in Figure 2c and the (211) facet in Figure S4 are due to the slight inclination in the edge of the BFO particles.

Therefore, the upper square surfaces perpendicular to the (200) and (020) facets are the (001) crystal facet, which is consistent with the enhanced (001) reflection in the XRD pattern suggesting a preferred orientation in [001] direction. In Figure 2f, the (001) and (110) crystal facets were observed, demonstrating that the surface of the BFO NPs by glycine combustion is perpendicular to the (001) crystal facet.

3.2. Facet Selective Deposition. BFO particles synthesized by the hydrothermal method were chosen as the raw material for facet-selective photo-deposition experiments including photo-reduction of Ag^+ and photo-oxidation of Mn^{2+}. The photo-reduction of Ag at the surfaces of BFO particles can be described as:[15]

$$Ag^+ + e^- \rightarrow Ag^0 \quad (3)$$

Similarly, the photo-oxidation of Mn^{2+} can be described as

$$2Mn^{2+} + 3H_2O + 2h^+ \rightarrow Mn_2O_3 + 6H^+ \quad (4)$$

Accordingly, Ag and Mn_2O_3 particles should be observed at the electron-rich or hole-rich surfaces, respectively.

Figure 3 shows the SEM and TEM images of BFO particles synthesized by hydrothermal before and after the facet-selective photo-deposition, the STEM of the Ag and Mn_2O_3 deposited BFO particles without irradiation, and a schematic diagram for the reaction process, respectively. According to the STEM image of the Ag deposited BFO particles shown in Figure 3a, small NPs appeared on the (200) facet of BFO particles, but not the (001) facet. In the TEM image of the Ag/BFO particles shown in Figure 3b, small NPs were also observed on the (200) surface only. The crystal plane spacing of the small NPs is measured to be 2.36 Å and 2.04 Å from the high resolution TEM image shown in Figure 3c, which can be indexed to (111) and (200) planes of Ag, which is expected based on the deposition process. To confirm the composition and the valence state of the

NPs deposited on the (200) surfaces of BFO particles, XPS spectra were measured and presented in Figure 4. The peaks at 368.0 eV and 374.1 eV in Figure 4a can be attributed to Ag $3d_{5/2}$ and $3d_{3/2}$ in its metallic state, confirming the small NPs observed being metallic silver.[15] The formation of Ag NPs suggests that Ag^+ ions accept photo-generated electrons and are photo-reduced from Ag^+.

For the Mn-deposited BFO particles revealed by SEM images shown in Figure 3d, small NPs with average diameter of about 20-30 nm were found on the (001) crystal facets of BFO particles. The corresponding XPS spectrum is shown in Figure 4b. The peaks located at 641.6 eV and 653.4 eV indicate the valence state of $3d_{5/2}$ and $3d_{3/2}$ of Mn^{3+}, instead of Mn^{2+}.[15] Therefore, the NPs on the (001) crystal facets of BFO particles can attributed to Mn_2O_3. The increase in oxidation state from Mn^{2+} to Mn^{3+} indicates that Mn^{2+} were photo-oxidized to Mn^{3+} on the (001) facets following light irradiation.

Together, the mechanism of facet selective deposition of Ag and Mn_2O_3 on the different surfaces of BFO particles is schematic illustrated as Figure 3g. Since BFO is ferroelectric, spontaneous polarization takes place in the BFO particles. Thus, positive or negative charges gather at different crystal facets of BFO particles. When BFO particles were exposed in light irradiation, photo-generated electron-hole pairs were first generated and then separated onto the (200) and (001) surface of the BFO particles, respectively. The Ag^+ ions act as acceptors of the photo-generated electrons, resulting in the deposition of Ag metal particles, while Mn^{2+} ions act as acceptors of the photo-generated holes, generating Mn_2O_3 particles. To further confirm the necessity of light irradiation, the STEM images of Ag and Mn_2O_3 deposited BFO particles without light irradiation are presented in Figures 3e and 3f. Comparing to Figure 3a, there is no nanoparticle deposited on the surface of BFO particles without light irradiation, demonstrating that the light is necessary for the selective deposition of Ag and Mn_2O_3 particles. And, it is the photo-generated electrons and

holes in BFO that initiate the deposition process.

In order to confirm the chemical nature of the NPs deposited onto the BFO surfaces, elemental mapping analysis was carried out and the results are shown in Figure 5. The images for Ag/BFO particles shown in Figure 5a reveal that Ag atoms were deposited as solid NPs on the {200} crystal facets of BFO under light irradiation. As can be seen in Figure 5b, Mn is less uniform compared to the distribution of Bi, indicating that Mn is concentrated as Mn_2O_3 NPs deposited on the {001} crystal facets of the BFO particles. The images in Figure 5c show that the Ag and Mn_2O_3 NPs were deposited on the {200} and {001} crystal facets of BFO particles, respectively. These results further confirm that the photo-generated electrons and holes can be effectively separated on the surfaces of BFO particles.

To obtain a small crystal size with large specific surface area, so as to increase the electrocatalytic efficiency, we prepared Ag/BFO NPs by glycine combustion synthesis followed by photo-deposition of Ag. Figure 6 shows the TEM, STEM images and the corresponding EDS elemental mapping images of Ag/BFO NPs by glycine combustion synthesis. The Ag/BFO NPs have near spherical shape with an average diameter of about 60 nm (Figure 6a). The high resolution STEM images (Figure 6b) and the diffraction spots (Figure 6c) of the BFO NPs show the same lattice constants as those in Figure 2. The surface of BFO NPs prepared by glycine combustion method is vertical to the (001) crystal facet, indicating that Ag can be deposited on the surface of BFO NPs. As shown in Figure 6d, many white highlighted regions were deposited onto the BFO surfaces, which were confirmed to be Ag clusters based on elemental mapping analysis (Figures 6e to 6h).

As an electrocatalytic material, the specific surface area has significant effect on its performance. To compare the specific surface areas of two kinds of Ag/BFO particles by different

methods, Ag NPs were deposited on the surface of two types of BFO particles under the same experimental conditions. The specific surface area of Ag/BFO particles was measured to be 1.68 ± 0.015 m^2/g and 5.29 ± 0.027m^2/g for the hydrothermal synthesis and glycine combustion, respectively, which indicates that the smaller BFO particles have larger specific surface area under the same Ag deposition conditions. Since the specific surface areas of the two BFO particles are different, it is hard to deposit the same amount of Ag on the Ag/BFO particles. The Ag content of Ag/BFO prepared by hydrothermal synthesis and Ag/BFO by glycine combustion was measured to be 0.063% and 0.21%, respectively. The Ag content is almost in direct proportion to the specific surface area. According to the study of Faber *et al*.,[33] it is reasonable to conclude that the Ag/BFO NPs prepared by glycine combustion with larger specific surface area and Ag content should have higher electrocatalytic activity than Ag/BFO prepared by hydrothermal synthesis. Thus, BFO NPs prepared using glycine combustion was employed for electrocatalytic study.

The stability of the Ag/BFO NPs was studied by characterizing their microstructure by STEM after eight months of storage (see Figure S5 in supplementary material). The results demonstrate that the Ag/BFO NPs are stable after long period of storage.

3.3. Electrocatalytic Properties and Mechanism of Enhancement. To study the effect of Ag modification on the electrocatalytic activities of BFO NPs, cyclic voltammetry (CV) measurements were conducted on different electrodes, including Nafion/GOD/GCE, Nafion/BFO/GOD/GCE, and Nafion/(Ag/BFO)/GOD/GCE, in PBS buffered solution towards glucose detection. As shown in Figure 7, the CV curve of the Nafion/GOD/GCE electrode shows no observable peak in 40 $\mu mol \cdot L^{-1}$ glucose in PBS. Compared to the electrode without BFO NPs, the current signal of the CV curve for the Nafion/BFO/GOD/GCE electrode (inset) shows only a small enhancement in the whole voltage range, which is still too weak for glucose detection. Interestingly, for the

Nafion/(Ag/BFO)/GOD/GCE electrode, the current intensity significantly increased, and two obvious peaks appeared at about 0.22 V and 0.52 V, which correspond to the oxidation peaks of glucose and H_2O_2 catalyzed on electrode, respectively.[25,34] Moreover, the current signal at 0.52 V is almost six times as large as that of the Nafion/BFO/GOD/GCE electrode. Therefore, the Ag/BFO NPs have a much better electrocatalytic activity for glucose detection than BFO NPs, which is attributable to Ag deposition.

The electrocatalytic enhancement mechanism of the Nafion/BFO/GOD/GCE electrode can be explained by the combined effects of the Fenton reaction[35] and the scavenging of conduction electrons. It has been reported that the addition of H_2O_2 into the aqueous suspensions of ferric oxides can enhance the catalytic activity by dissolved iron species, which is named the Fenton reaction (Equations 7 and 8). The reaction process can be described as follows:[36]

$$H_2O_2 + Bi_2Fe_4O_9 \rightarrow {}^{\bullet}OH + OH^- \quad (5)$$

$$FeOH^{2+} \xrightarrow{hv} Fe^{2+} + {}^{\bullet}OH \quad (6)$$

$$Fe^{2+} + H_2O_2 \rightarrow Fe^{3+} + {}^{\bullet}OH + OH^- \quad (7)$$

$$Fe^{3+} + H_2O_2 \rightarrow Fe^{2+} + HO_2^{\bullet} + H^+ \quad (8)$$

Therefore, the electrode with BFO NPs may have a higher efficiency in decomposing H_2O_2, producing ·OH that can oxidize glucose in the solution. As a result, the electrode shows good electrocatalytic activity towards glucose as indicated by the current signal in the CV curves.

The higher electrocatalytic activity of the Nafion/(Ag/BFO)/GOD/GCE electrode compared to the Nafion/BFO/GOD/GCE electrode is clearly related to the Ag deposition. Considering the conductivity is an important factor to the electrocatalytic activity, alternating current (AC) impedance curves of BFO NPs and Ag/BFO NPs were measured to determine the difference in resistance and electron transport, as shown in Figure 8. Based on the diameter of the impedance

semicircle, the impedance of BFO NPs (1.5×10^4 ohm) is about 2.7 times as that of Ag/BFO NPs (5.5×10^3 ohm). Hence, the Ag/BFO NPs have larger conductivity than BFO NPs, which can enhance electron transport in the electrocatalytic process and result in improved electrocatalytic activity.

Since the magnetic property of NPs may affect their electron transport, the hysteresis loops of BFO and Ag/BFO NPs have been measured at room temperature to understand their magnetic properties and possible relation to the electrocatalytic properties, shown in Figure 9. Interestingly, enhanced ferromagnetism was observed after the Ag deposition on BFO NPs. Bulk BFO is paramagnetic at room temperature, and its Nẽel temperature is 264 K, below which weak antiferromagnetism has been detected.[33,37] However, BFO NPs show a weak ferromagnetic behavior with a coercivity (H_C) of about 74 Oe and a remanence (M_r) of about 0.0132 emu/g. The origin of the ferromagnetism in BFO NPs could be regarded as a core-shell magnetic structure with antiferromagnetic inner cores and ferromagnetic surfaces.[38,39] After the Ag deposition, the ferromagnetism of Ag/BFO NPs shows an obvious enhancement with M_r of about 0.060 emu/g. However, H_C has no obvious change after the Ag deposition, which indicates that the origin of the ferromagnetism is identical between the two types of NPs. The higher M_r of Ag/BFO NPs should be due to the Ag NPs on the surfaces.[40,41] The enhanced ferromagnetism may be correlated with the improved electron transport for Ag/BFO NPs, which is a key factor for electrocatalytic activity. In the ferromagnetic Ag/BFO NPs, the magnetic moments are all in parallel alignment. Therefore, it is much easier for the electrons in the majority spin direction to transport. Therefore, the resistance decreases in the ferromagnetic Ag/BFO NPs. The fast electron transport in Ag/BFO NPs increases the electrocatalytic efficiency. Therefore, the enhanced electrocatalytic activity of Ag/BFO NPs may also be related to spin dependent charge transport that is improved due to a combination of Ag

deposition and spin alignment.

3.4. Biosensing Activity. The biosensing activity of Ag/BFO NPs was studied with CV measurements using the Nafion/(Ag/BFO)/GOD/GCE electrode in PBS buffer with 40 $\mu mol \cdot L^{-1}$ glucose at various scan rates from 0.0050 to 0.16 V/s, as shown in Figure 10a. As the scan rate increases, the corresponding oxidation peak currents in the CV curves increase along with a gradual potential shift of the oxidation peak to the positive direction as the scan rate increases, which is similar to a previous study on glucose sensor.[25] Figure 10b shows the oxidation peak current as a function of scan rate. The peak current is linearly proportional to the scan rate over the potential range with a correlation coefficient (R^2) of 0.9922, which is a typical diffusion controlled surface electrochemical behavior.[42,43]

To study the glucose sensitivity of the Nafion/(Ag/BFO)/GOD/GCE electrode, the CV curves have also been measured at different concentrations of glucose (Figure 11a), and the absolute current values at the peaks drawn from Figure 11a are plotted as a function of glucose concentration (Figure 11b). The absolute current values at the H_2O_2 oxidation peaks decrease with the concentration of glucose decreasing from 200 to 5.0 $\mu mol \cdot L^{-1}$. As shown in the Figure 11b, the current value varies linearly with the glucose concentration. The data of the maximum current changes can be linearly fit as:

$$I\ (\mu A) = 5.81532 + 0.01714C\ (\mu mol \cdot L^{-1}), \quad (9)$$

where I is the current value, and C is the glucose concentration. R^2 for the linear simulation is 0.9988. The sensitivity of the biosensor for glucose detection is calculated to be 87.3 $\mu A \cdot mmol^{-1} \cdot L \cdot cm^{-2}$. If one sets the Signal Noise Ratio as 3:1, the minimum detection limit of the electrode is 0.50 $\mu mol \cdot L^{-1}$. Compared to previously reported glucose biosensors[44-51] (see Table 1), the Nafion/(Ag/BFO)/GOD/GCE electrode has a relatively low detection limit and a high sensitivity

for glucose detection, which meets the requirements for high sensitivity glucose monitoring.

4. CONCLUSIONS

Ag/BFO NPs have been synthesized using Ag deposition under visible light irradiation on BFO NPs prepared by glycine combustion. The crystal structure and chemical nature of the Ag/BFO NPs were characterized by XRD, TEM, STEM and XPS. The electrocatalytic activity of Ag/BFO NPs was demonstrated using enzymatic glucose detection with an amperometric biosensor, which shows a limit of detection limit, high sensitivity, and good linearity in the range of 5.0~200 $\mu mol \cdot L^{-1}$. Compared to electrodes modified by different NPs, the Ag deposition on the surface of BFO NPs significantly enhanced the electrocatalytic activity. Comparative experiments of Mn^{2+} oxidation reaction on BFO NPs were carried out to explain the origin of the electrocatalytic enhancement by Ag deposition. It was found that Ag^{+} reduction and Mn^{2+} oxidation reactions take places at {200} and {001} facet, respectively. The facet-specific reactivity is intriguing and potentially useful for chemical reactions that desire product selectivity. Based on the high conductivity of Ag/BFO NPs, effective charge separation on the BFO NP surfaces is likely responsible for the enhanced electrocatalytic activity. Moreover, ferromagnetism was enhanced after the Ag deposition on BFO NPs, and spin-dependent transport may be related to the improved electrocatalytic properties. Accordingly, the demonstrated high electrocatalytic activity of Ag/BFO NPs shows great promise for biosensing as well as chemical synthesis applications.

■ ASSOCIATED CONTENT

Supporting Information

X-ray Rietveld refinements of the BFO NPs and Ag/BFO NPs synthesized by glycine combustion and the refined crystallographic parameters. The HRTEM images and the diffraction spots of the BFO particles synthesized by hydrothermal method. The STEM image of the Ag/BFO NPs using

glycine combustion method after storage for 8 months.

■ AUTHOR INFORMATION

Corresponding Author

* E-mail: xgxu@ustb.edu.cn.

* E-mail: yjiang@ustb.edu.cn.

Notes

The authors declare no competing financial interest.

■ ACKNOWLEDGMENTS

This work was partially supported by the National Basic Research Program of China (Grant No. 2015CB921502), the National Science Foundation of China (Grant Nos. 51671019, 51471029, 51731003, 61471036, 11574027) and Beijing science and technology Nova cross program (Z171100001117136). JZZ is grateful to support from the UCSC Senate COR special research fund.

REFERENCES

(1) MacKenzie, K. J. D.; Dougherty, T.; Barrel, J. The electronic properties of complex oxides of bismuth with the mullite structure. *J. Eur. Ceram. Soc.*, **2008**, *28*, 499-504.

(2) Yang, H. B.; Dai, J. J.; Wang, L.; Lin, Y. A novel approach to prepare $Bi_2Fe_4O_9$ flower-like spheres with enhanced photocatalytic performance. *Sci. Rep.*, **2017**, *7*, 768.

(3) Zhang, X. Y.; Bourgeois, L.; Yao, J. F.; Wang, H. T.; Webley, P. A. Tuning the morphology of bismuth ferrite nano- and microcrystals: From sheets to fibers. *Small*, **2007**, *3*, 1523-1528.

(4) Koizumi, H.; Niizeki, N.; Ikeda, T. An X-ray study on Bi_2O_3-Fe_2O_3 system. *Jpn. J. Appl. Phys.*, **1964**, *3*, 495-496.

(5) Park, T. J.; Papaefthymiou, G. C.; Moodenbaugh, A. R.; Mao, Y.; Wong, S. S. Synthesis and characterization of submicron single-crystalline $Bi_2Fe_4O_9$ cubes. *J. Mater. Chem.*, **2005**, *15*, 2099-2105.

(6) Murshed, M. M.; Nénert, G.; Burianek, M.; Robben, L.; Mühlberg, M.; Schneider, H.; Reinhard X. Fischer, R. X.; Gesing, T. M. Temperature-dependent structural studies of mullite-type $Bi_2Fe_4O_9$. *J. Solid State Chem.*, **2013**, *197*, 370-378.

(7) Curti, M.; Gesing, T. M.; Murshed, M. M.; Bredow, T.; Mendive, C. B. Liebau density vector: a new approach to characterize lone electron pairs in mullite-type materials. *Z. Kristallogr.*, **2013**, *228*, 629-634.

(8) Kostiner, E.; Shoemaker, G. L. Mössbauer effect study of $Bi_2Fe_4O_9$. *J. Solid. State. Chem.*, **1971**, *3*, 186-189.

(9) Groult, D.; Hervieu, M.; Nguyen, N.; Raveau, B. GeV-xenon ion latent tracks in $Bi_2Fe_4O_9$: Mössbauer and electron microscopy studies. *J. Solid. State. Chem.*, **1988**, *76*, 248-259.

(10) Poghossian, A. S.; Abovian, H. V.; Avakian, P. B.; Mkrtchian, S. H.; Haroutunian, V. M.

Bismuth ferrites: New materials for semiconductor gas sensors. *Sens. Actuators. B*, **1991**, *4*, 545-549.

(11) Zakharchenko, N. I. Catalytic properties of the Fe_2O_3-Bi_2O_3 system in ammonia oxidation to nitrogen oxides. *Kinet. Cataly.*, **2002**, *43*, 95-98.

(12) Hu, Z. T.; Lua, S. K.; Lim, T. T. Cuboid-like $Bi_2Fe_4O_9$/Ag with graphene-wrapping tribrid composite with superior capability for environmental decontamination: nanoscaled material design and visible-light-driven multifunctional catalyst. *ACS Sustain. Chem. Eng.*, **2015**, *3*, 2726-2736.

(13) Gu, L.; Song, F.; Zhu, N. An Innovative Electrochemical Degradation of 1-Diazo-2-Naphthol-4-Sulfonic Acid in the Presence of $Bi_2Fe_4O_9$. *Appl. Catal. B*, **2011**, *110*, 186-194.

(14) Kirsch, A.; Murshed, M. M.; Schowalter, M.; Rosenauer, A.; Gesing, T. M. Nanoparticle Precursor into Polycrystalline $Bi_2Fe_4O_9$: An Evolutionary Investigation of Structural, Morphological, Optical, and Vibrational Properties. *J. Phys. Chem. C*, **2016**, *120*, 18831-18840.

(15) Li, R. G.; Zhang, F. X.; Wang, D. G.; Yang, J. X.; Li, M. R.; Zhu, J.; Zhou, X.; Han, H. X.; Li, C. Spatial separation of photo generated electrons and holes among {010} and {110} crystal facets of $BiVO_4$. *Nat. Commun.*, **2013**, *4*, 1432.

(16) Wang, L. L.; Jackman, J. A.; Ng, W. B.; Cho, N. J. Flexible, Graphene-Coated Biocomposite for Highly Sensitive, Real-Time Molecular Detection. *Adv. Funct. Mater.*, **2016**, *26*, 8623-8630.

(17) Li, Y.; Zhang, P. P.; Ouyang, Z. F.; Zhang, M. F.; Lin, Z. J.; Li, J. F.; Su Z. Q.; Wei, G. Nanoscale Graphene Doped with Highly Dispersed Silver Nanoparticles: Quick Synthesis, Facile Fabrication of 3D Membrane-Modified Electrode, and Super Performance for Electrochemical Sensing. *Adv. Funct. Mater.*, **2016**, *26*, 2122-2134.

(18) Kong, C. C.; Tang, L. L.; Zhang, X. Z.; Sun, S. D.; Yang, S. C.; Song X. P.; Yang, Z. M. Templating synthesis of hollow CuO polyhedron and its application for nonenzymatic glucose detection. *J. Mater. Chem. A*, **2014**, *2*, 7306-7312.

(19) Giri, A. K.; Charan, C.; Saha, A.; Shahib V. K.; Panda, A. B. An amperometric cholesterol biosensor with excellent sensitivity and limit of detection based on an enzyme-immobilized microtubular ZnO@ZnS heterostructure. *J. Mater. Chem. A*, **2014**, *2*, 16997-17004.

(20) Zhao, S.; You, B.; Jiang, L. Oriented Assembly of Zinc Oxide Mesocrystal in Chitosan and Applications for Glucose Biosensors. *Cryst. Growth. Des.*, **2016**, *16*, 3359-3365.

(21) Zhang, Y. Y.; Wang, L.; Yu, J.; Yang, H.; Pan, G. X.; Miao, L. F.; Song, Y. H. Three-Dimensional Macroporous Carbon Supported Hierarchical ZnO-NiO Nanosheets for Electrochemical Glucose Sensing. *J. Alloy. Compd.*, **2017**, *698*, 800-806.

(22) Bai, S.; Wu, W. W.; Qin, Y.; Cui, N. Y.; Bayerl**,** D. J.; Wang, X. D. High-Performance Integrated ZnO Nanowire UV Sensors on Rigid and Flexible Substrates. *Adv. Funct. Mater.*, **2011**, *21*, 4464-4469.

(23) Yin, H.; Zhang, C. Z.; Liu F.; Hou, Y. L. Hybrid of Iron Nitride and Nitrogen-Doped Graphene Aerogel as Synergistic Catalyst for Oxygen Reduction Reaction. *Adv. Funct. Mater.*, **2014**, *24*, 2930-2937.

(24) Zou, J.; Jiang, J.; Zhang, Y.; Ma, J.; Wan, Q. A comparative study of the optical, magnetic and electrocatalytic properties of nano $BiFeO_3$ with different morphologies. *Mater. Lett.*, **2012**, *72*, 134-136.

(25) Huo, H. H.; Xu, Z. D.; Zhang T.; Xu, C. L. Ni/CdS/TiO_2 nanotube array heterostructures for high performance photoelectrochemical biosensing. *J. Mater. Chem. A*, **2015**, *3*, 5882-5888.

(26) Ibupoto, Z. H.; Tahira, A.; Mallah, A. B.; Shahzad, S. A.; Willander, M.; Wang, B.; Yu C. The

Synthesis of Functional Cobalt Oxide Nanostructures, and their Sensitive Glucose Sensing Application. *Electroanal.*, **2017**, *29*, 213-222.

(27) Rakhi, R. B.; Sethupathi, K.; Ramaprabhu, S. A glucose biosensor based on deposition of glucose oxidase onto crystalline gold nanoparticle modified carbon nanotube electrode. *J. Phys. Chem. B*, **2009**, *113*, 3190-3194.

(28) Poscia, A.; Mascini, M.; Moscone, D.; Luzzana, M.; Caramenti, G.; Cremonesi, P.; Valgimigli, F.; Bongiovanni C.; Varalli M. A microdialysis technique for continuous subcutaneous glucose monitoring in diabetic patients. *Biosens. Bioelectron.*, **2003**, *18*, 891-898.

(29) Du, W.; Xu, Y.; Wang, Y. Photo induced degradation of orange II on different iron (Hydr) oxides in aqueous suspension: Rate enhancement on addition of hydrogen peroxide, silver nitrate, and sodium fluoride. *Langmuir*, **2008**, *24*, 175-181.

(30) Ruan, Q. J.; Zhang, W. D. Tunable morphology of $Bi_2Fe_4O_9$ crystals for photocatalytic oxidation. *J. Phys. Chem. C*, **2009**, *113*, 4168-4173.

(31) Han, J. T.; Huang, Y. H.; Wu, X. J.; Wu, C. L.; Wei, W.; Peng, B.; Huang, W.; Goodenough, J. B. Tunable synthesis of bismuth ferrites with various morphologies. *Adv. Mater.*, **2006,** *18*, 2145-2148.

(32) Wu, X. H.; Miao, J.; Zhao, Y.; Meng, X. B.; Xu, X. G.; Wang S. G.; Jiang Y. Novel multiferroic $Bi_2Fe_4O_9$ nanoparticles: the interesting optical, photocatalytic, and multiferroic properties. *Optoelectron. Adv. Mater.*, **2013**, *7*, 116-120.

(33) Faber, M. S.; Dziedzic, R.; Lukowski, M. A.; Kaiser, N. S.; Ding, Q.; Jin, S. High-performance electrocatalysis using metallic cobalt pyrite (CoS_2) micro-and nanostructures. *J. Am. Chem. Soc.*, **2014**, *136*, 10053-10061.

(34) Zhang H.; Liu S. Nanoparticles-assembled NiO nanosheets templated by grapheneoxide film

for highly sensitive non-enzymatic glucose sensing. *Sensor Actuat. B-Chem.*, **2017**, *238*, 788-794.

(35) Xu, Z. H.; Hou, Y. L.; Sun, S. H. Magnetic core/shell Fe_3O_4/Au and Fe_3O_4/Au/Ag nanoparticles with tunable plasmonic properties. *J. Am. Chem. Soc.*, **2007**, *129*, 8698-8699.

(36) Sun, S. M.; Wang, W. Z.; Zhang, L.; Shang, M. Visible light-induced photocatalytic oxidation of phenol and aqueous ammonia in flowerlike $Bi_2Fe_4O_9$ suspensions. *J. Phys. Chem. C*, **2009**, *113*, 12826-12831.

(37) Tian, Z. M.; Qiu, Y.; Yuan, S. L.; Wu, M. S.; Huo S. X.; Duan, H. N. Enhanced multiferroic properties in Ti-doped $Bi_2Fe_4O_9$ ceramics. *J. Appl. Phys.*, **2010**, *108*, 064110.

(38) Bi, H.; Li, S. D.; Zhang, Y. C.; Du, Y. W. Ferromagnetic-like behavior of ultrafine NiO nanocrystallites. *J. Magn. Magn. Mater.*, **2004**, *277*, 363-367.

(39) Berkowitz, A. E.; Lahut J. A.; Jacobs, I. S.; Levinson, L. M.; Forester, D. W. Spin Pinning at Ferrite-Organic Interfaces. *Phys. Rev. Lett.*, **1975**, *34*, 594-597.

(40) Lu, L. Y.; Zhang, W. T.; Wang, D.; Xu, X. G.; Miao J.; Jiang, Y. Fe@Ag core–shell nanoparticleswith both sensitive plasmonic properties and tunable magnetism. *Mater. Lett.*, **2010**, *64*, 1732-1734.

(41) Cao, Y. W.; Jin, R. C.; Mirkin, C. A. DNA-Modified Core−Shell Ag/Au Nanoparticles. *J. Am. Chem. Soc.*, **2001**, *123*, 7961-7962.

(42) Lei, Y.; Luo, N.; Yan, X. Q.; Zhao, Y. G.; Zhang G.; Zhang, Y. A highly sensitive electrochemical biosensor based on zinc oxide nanotetrapods for L-lactic acid detection. *Nanoscale*, **2012**, *4*, 3438-3443.

(43) Wang, J. X.; Sun, X. W.; Wei, A.; Lei, Y.; Cai, X. P.; Li, C. M.; Dong Z. L. Zinc oxide nanocomb biosensor for glucose detection. *Appl. Phys. Lett.*, **2006**, *88*, 233106.

(44) Liu, H.; Tao, C. A.; Hu, Z.; Zhang, S.; Wang, J.; Zhan, Y. An electrochemical glucose biosensor based on graphene composites: use of dopamine as reducing monomer and as site for covalent immobilization of enzyme. *RSC Adv*., **2014**, *4*, 43624−43629.

(45) Liu, X.; Ai, L.; Jiang, J. Interconnected porous hollow CuS microspheres derived from metal-organic frameworks for efficient adsorption and electrochemical biosensing. *Powder Technol.*, **2015**, *283*, 539–548.

(46) Mei, L.; Zhang, P.; Chen, J.; Chen, D.; Quan, Y.; Gu, N.; Zhang, G.; Cui, R. Non-enzymatic sensing of glucose and hydrogen peroxideusing a glassy carbon electrode modified with a nanocomposite consisting of nanoporous copper, carbon black and nafion. *Microchim. Acta*, **2016,** *183*, 1359–1365.

(47) Guan, P.; Li, Y.; Zhang, J.; Li, W. Non-enzymatic glucose biosensor based on CuO-decorated CeO_2 nanoparticles. *Nanomaterials*, **2016**, *6*,159.

(48) Chang, G.; Shu, H.; Huang, Q.; Oyama, M.; Ji, K.; Liu, X.; He, Y. Synthesis of highly dispersed Pt nanoclusters anchored graphene composites and their application for non-enzymatic glucose sensing. *Electrochim. Acta*, **2015**, *157*,149–157.

(49) Heidari, H.; Habibi, E. Amperometric enzyme-free glucose sensor based on the use of a reduced graphene oxide paste electrode modified with electrodeposited cobalt oxide nanoparticles. *Microchim. Acta*, **2016**, *183*, 2259–2266.

(50) Yang, S.; Li, G.; Wang, G.; Zhao, J.; Gao, X.; Qu, L. Synthesis of Mn_3O_4 nanoparticles/ nitrogen-doped graphene hybrid composite for nonenzymatic glucose sensor. *Sens. Actuators, B-Chem*, **2015**, *221*,172–178.

(51) Song, Y.; Wei, C.; He, J.; Li, X.; Lu, X.; Wang, L. Porous Co nanobeads/rGO nanocomposites derived from rGO/Co-metal organic frameworks for glucose sensing. *Sens. Actuators, B-Chem*,

2015, *220*, 1056–1063.

Table Captions

Table 1. Performance comparison of Ag/BFO NPs based biosensor with previously reported glucose biosensors.

Sensor Electrodes	Sensitivity ($\mu A \cdot mmol^{-1} \cdot L \cdot cm^{-2}$)	Linear Range ($mmol \cdot L^{-1}$)	Detection limit ($\mu mol \cdot L^{-1}$)	Ref
Ag/BFO NPs	87.3	0.005-0.20	0.50	Present study
PDA-RGD/GOD/PtNPs	33.0	0.20-1.0	100	44
Hollow CuS microsphere	65.0	0.010-1.55	3.78	45
Nanoporous copper	33.8	0.0060-3.37	2.6	46
CuO/CeO_2/ITO	2.77	Up to 4.0	10	47
Pt nanoclusters/graphene	1.21	1.0-25	30	48
Cobalt oxide NP/rGO	1.21	0.040-4.0	1.44	49
Mn_3O_4 NP/N-GR/CPE	101.1	Up to 0.53	1.0	50
Co nanobeads/rGO	39.3	0.15-6.25	47.5	51

Figure Captions

Figure 1. XRD patterns of the BFO particles synthesized by hydrothermal method and glycine combustion synthesis and the Ag/BFO NPs prepared using BFO NPs precursor synthesized by glycine combustion.

Figure 2. TEM images of the BFO particles synthesized by (a) hydrothermal method and (b) glycine combustion synthesis. (c) and (d) are high resolution TEM images for the BFO particles in panels (a) and (b), respectively. (e) and (f) are the diffraction spots of the BFO particles in panels (a) and (b), respectively.

Figure 3. (a) STEM of the BFO particles synthesized by hydrothermal method. (b) TEM of the Ag deposited BFO particles synthesized under light irradiation. (c) High resolution TEM of the nanoparticle on the surface of BFO particles in panel (b). (d) SEM of the Mn_2O_3 deposited BFO particles synthesized under light irradiation. (e) STEM of the Ag deposited BFO particles without light irradiation. (f) STEM of the Mn_2O_3 deposited BFO particles without light irradiation. (g) Schematic diagram of facets selective photo-deposition of Ag and Mn_2O_3 on the surface of BFO particles.

Figure 4. (a) Ag 3d and (b) Mn 3d XPS spectra of the Ag/BFO particles and Mn_2O_3/BFO particles with BFO particles precursor prepared using hydro-thermal synthesis.

Figure 5. STEM image with high angle annular dark field (STEM-HAADF) and corresponding EDS elemental mapping images of (a) Ag/BFO particles, (b) Mn_2O_3/BFO particles and (c) Ag and Mn_2O_3 co-deposited BFO particles, where the BFO particles precursor is prepared using hydro-thermal synthesis.

Figure 6. (a) TEM image of Ag/BFO NPs by glycine combustion synthesis. (b) The high resolution STEM image and (c) the diffraction spots of the BFO NPs. (d-h) The corresponding

STEM and EDS elemental mapping images of Ag/BFO NPs.

Figure 7. CV curves of the electrodes including Nafion/GOD/GCE, Nafion/GOD/BFO/GCE and Nafion/GOD/(Ag/BFO)/GCE in PBS with the glucose concentration of 40 μmol·L^{-1}. The inset shows the enlarged part of CV curves. The error of the data is 0.20% for CV curves from the equipment.

Figure 8. AC impedance diagrams of BFO NPs and Ag/BFO NPs.

Figure 9. Hysteresis loops of the BFO NPs synthesized by glycine combustion method before and after the Ag deposition.

Figure 10. (a) CV curves of the Nafion/GOD/(Ag/BFO)/GCE electrode in the PBS with the glucose concentration of 40 μmol·L^{-1} at various scan rates of 0.0050, 0.010, 0.030, 0.050, 0.10 and 0.16 V/s. (b) The oxidation peak current as a function of scan rate (line and symbol) and the linearly simulated results (line) with the correlation coefficient (R^2) of 0.9922.

Figure 11. (a) CV curves of the Nafion/GOD/(Ag/BFO)/GCE electrode in the PBS with different glucose concentration varying from 5.0 to 200 μmol·L^{-1}. (b) The relationship between the current peak and the glucose concentration, which can be linearly fit using I (μA) = 5.81532 +0.01714C (μmol·L^{-1}) with the correlation coefficient (R^2) of 0.9988.

Figure 1. (Wang K. *et al.*)

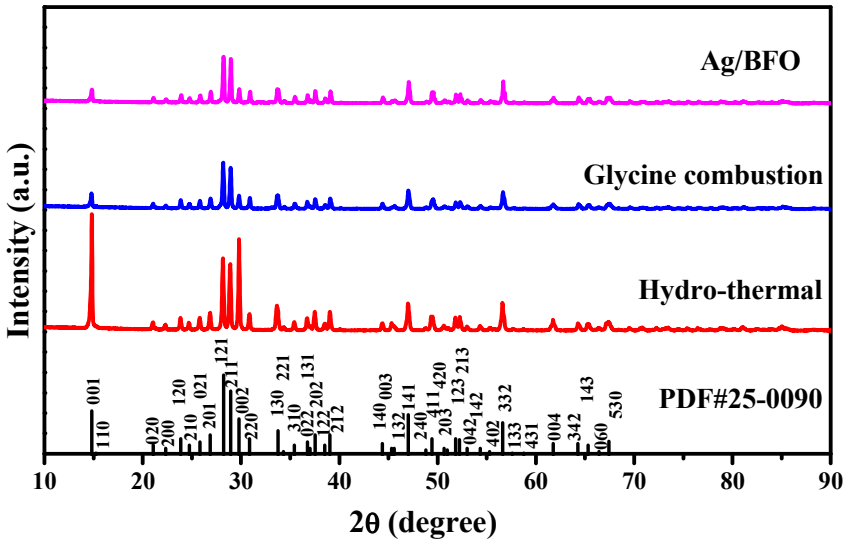

Figure 2. (Wang K. *et al.*)

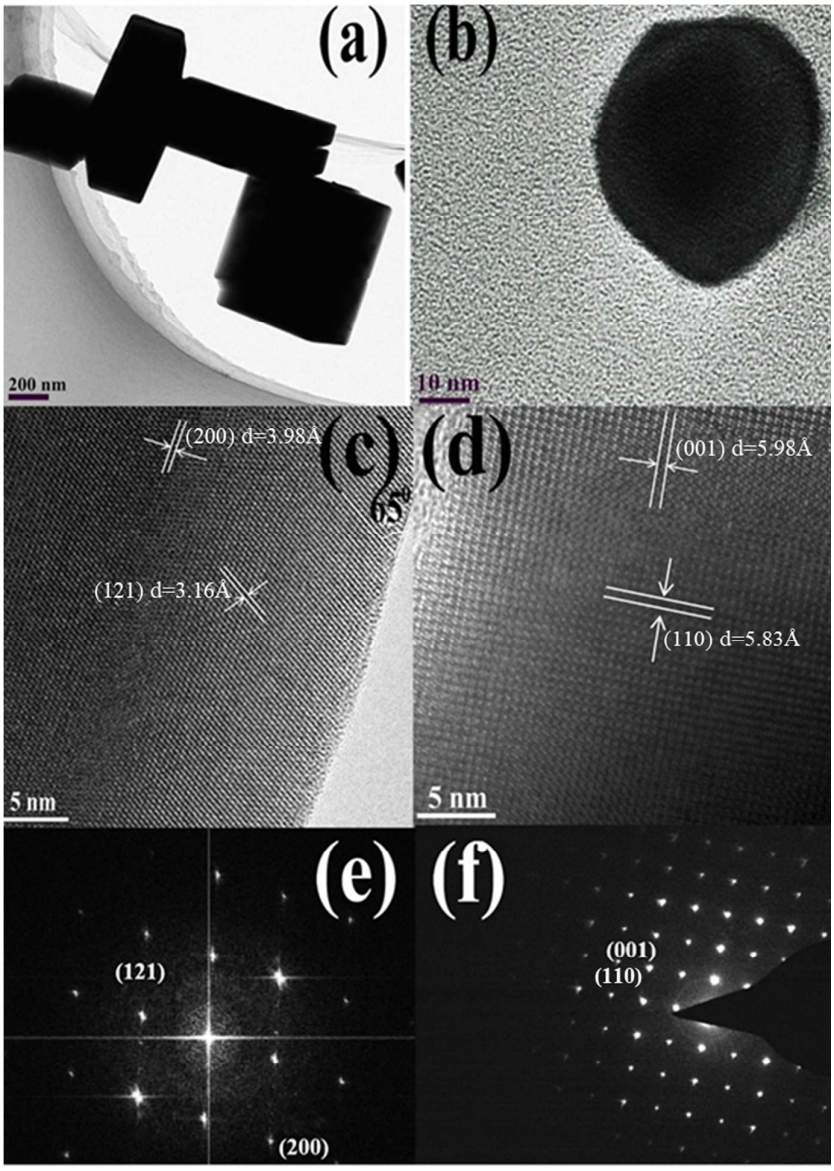

Figure 3. (Wang K. *et al.*)

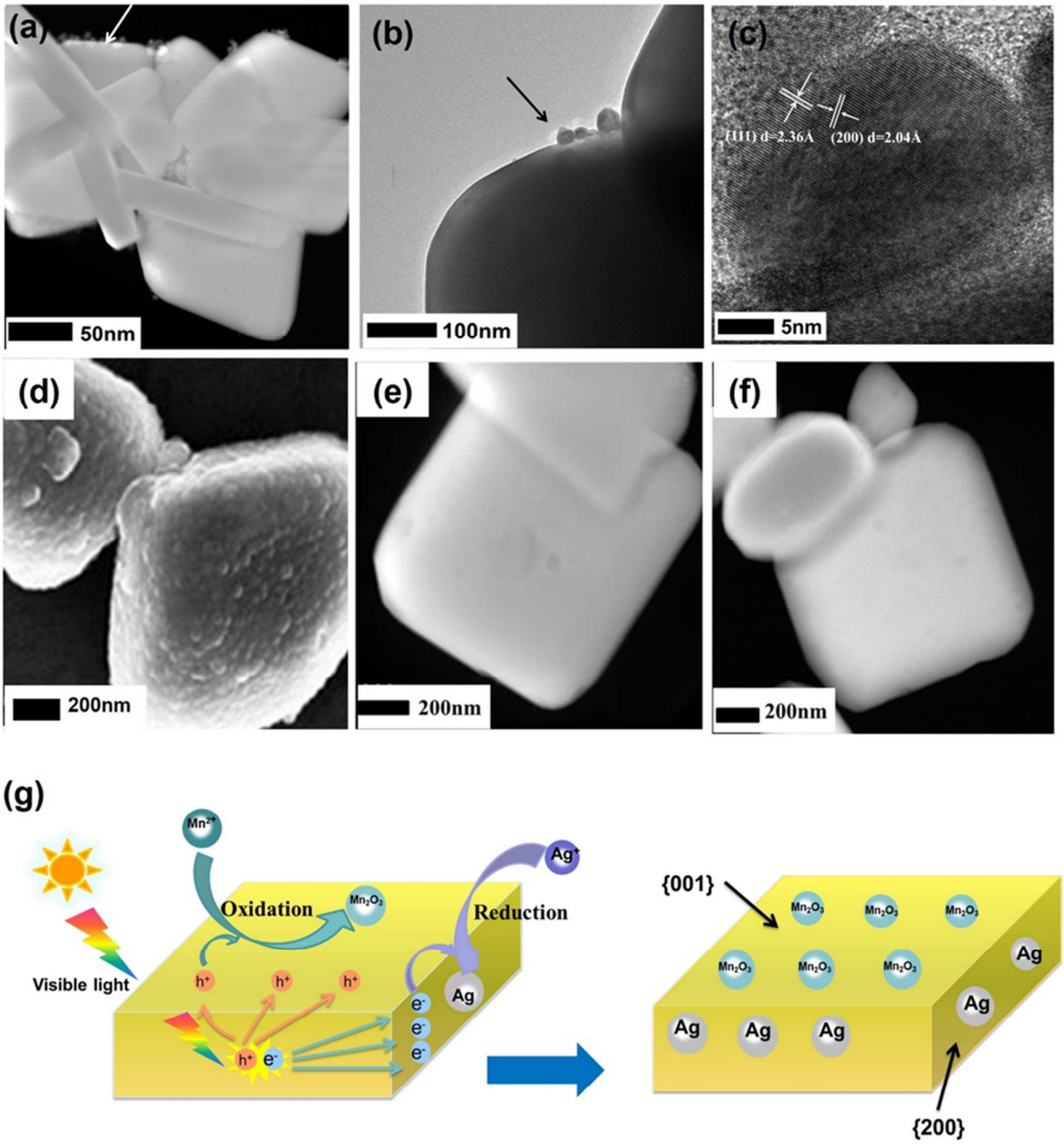

Figure 4. (Wang K. *et al.*)

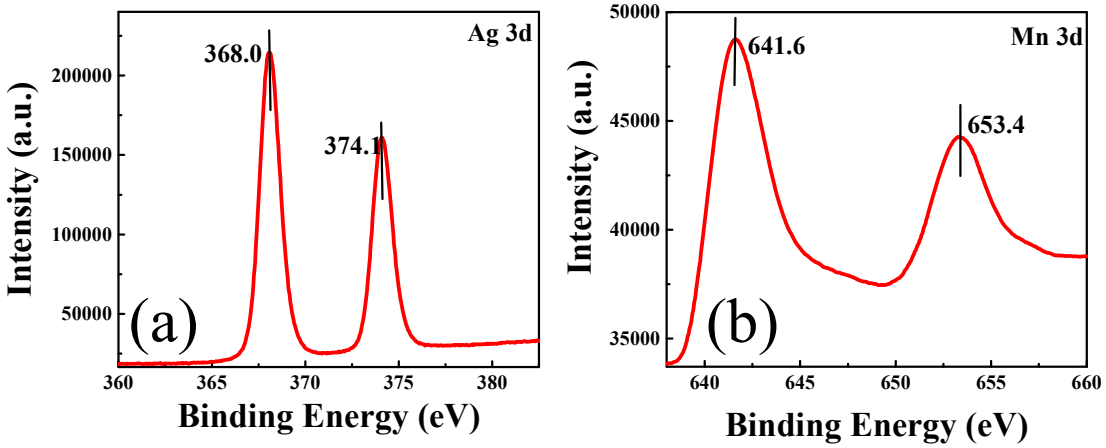

Figure 5. (Wang K. *et al.*)

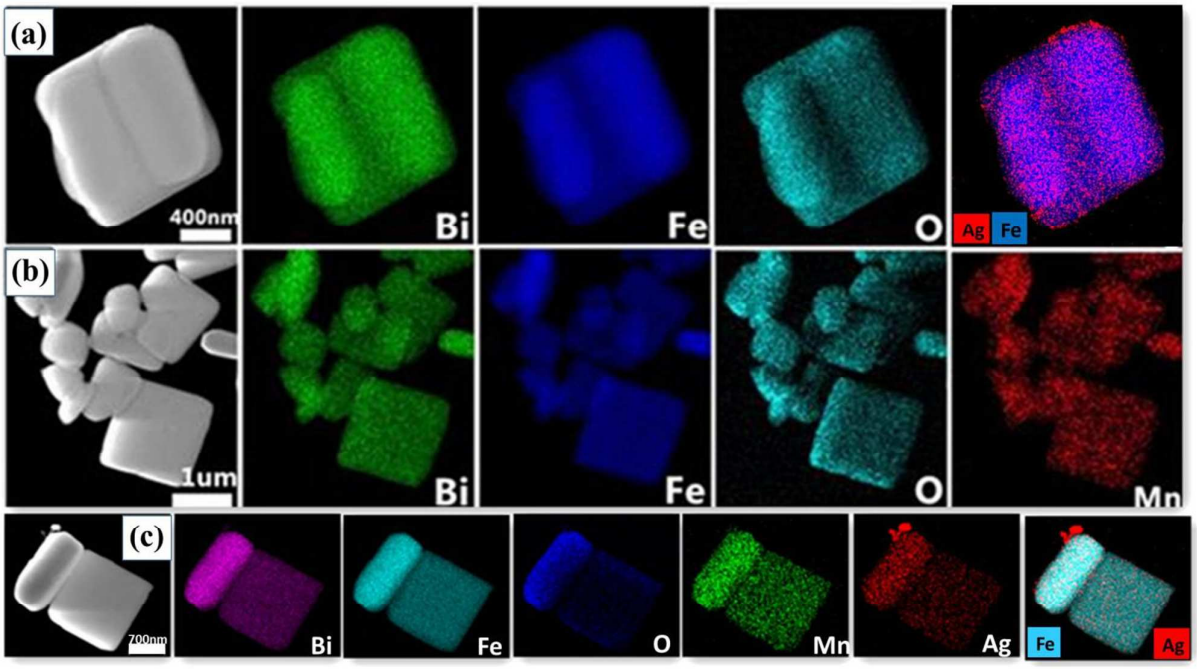

Figure 6. (Wang K. *et al.*)

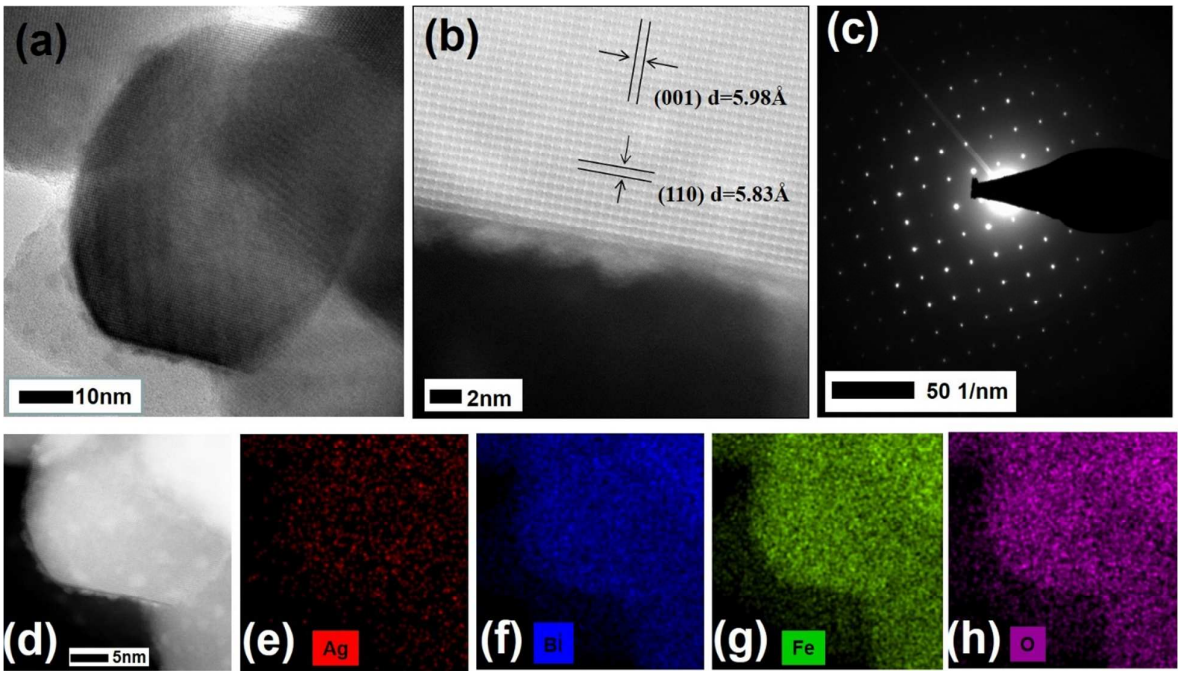

Figure 7. (Wang K. *et al.*)

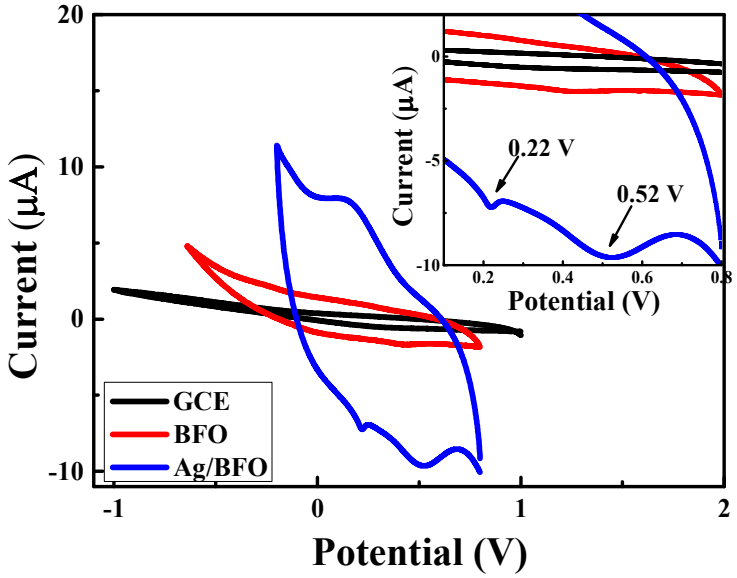

Figure 8. (Wang K. *et al.*)

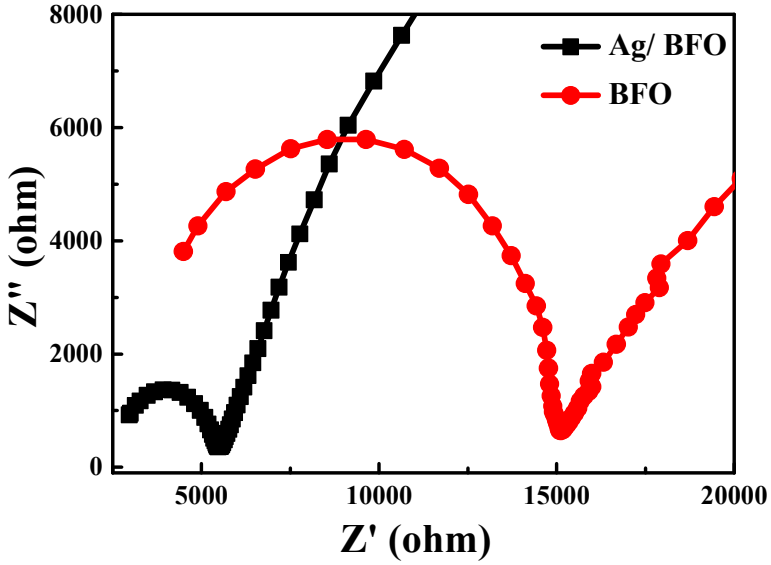

Figure 9. (Wang K. *et al.*)

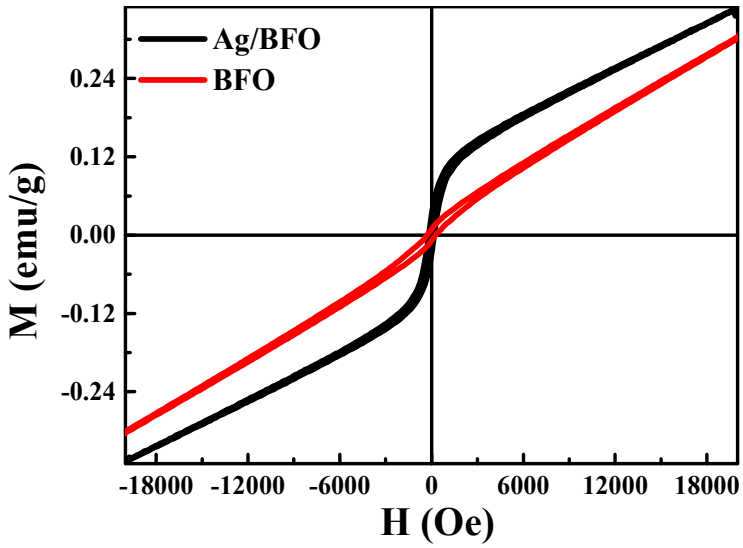

Figure 10. (Wang K. *et al.*)

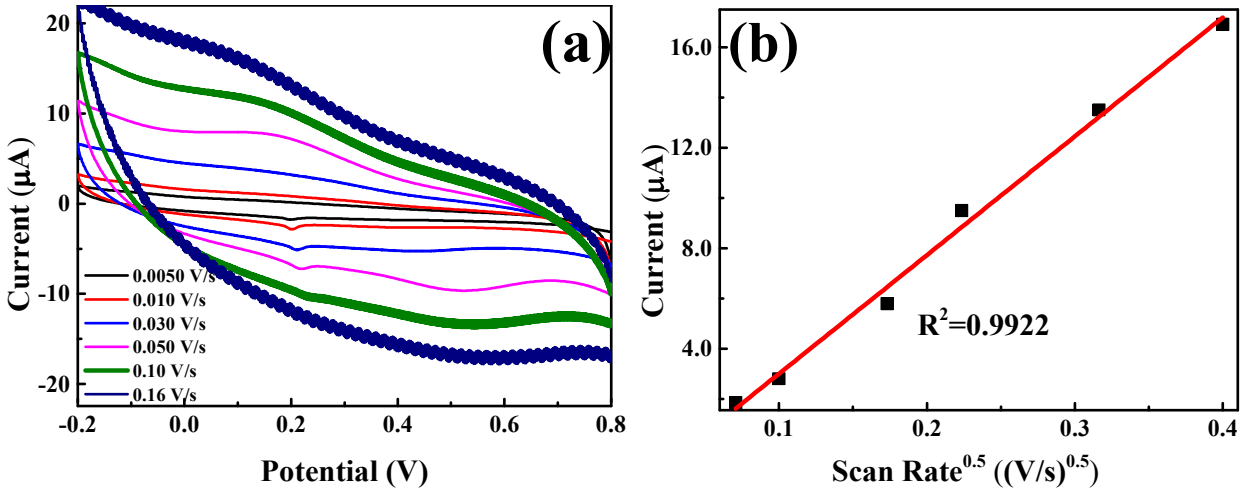

Figure 11. (Wang K. *et al.*)

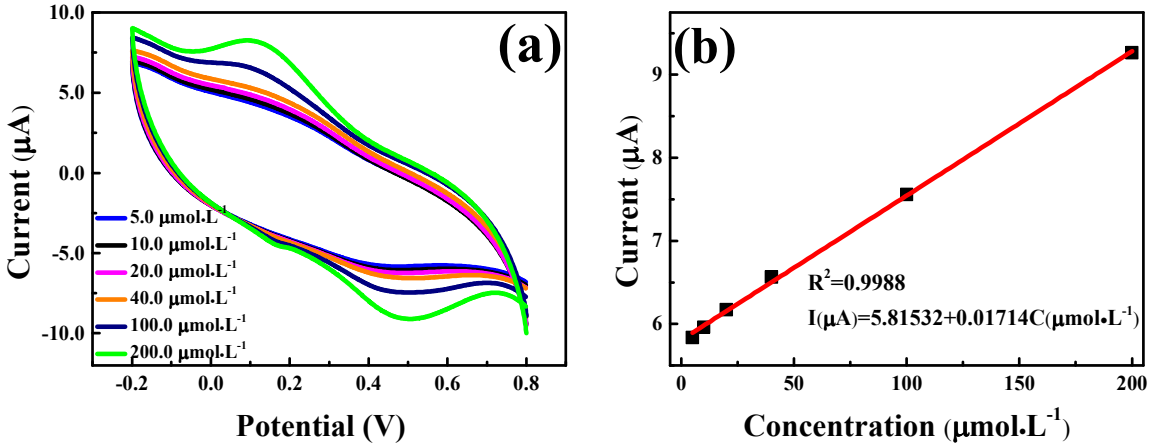

Table of Contents Graphic. (Wang K. *et al.*)